HHS Public Access

Author manuscript

Mol Imaging Biol. Author manuscript; available in PMC 2015 December 01.

Published in final edited form as:

Mol Imaging Biol. 2015 December ; 17(6): 848–855. doi:10.1007/s11307-015-0858-0.

Dual-Modality Optical/PET Imaging of PARP1 in Glioblastoma

Giuseppe Carlucci[1], **Brandon Carney**[1,2,3], **Christian Brand**[1], **Susanne Kossatz**[1], **Christopher P. Irwin**[1], **Sean D. Carlin**[1], **Edmund J. Keliher**[4], **Wolfgang Weber**[1,5], and **Thomas Reiner**[1,5]

[1]Department of Radiology, Memorial Sloan Kettering Cancer Center, 1275 York Avenue, New York, NY, 10065, USA

[2]Department of Chemistry and Biochemistry, Hunter College of the City University of New York, New York, NY, 10065, USA

[3]Ph.D. Program in Chemistry, The Graduate Center of the City University of New York, New York, 10018, USA

[4]Center for Systems Biology, Massachusetts General Hospital, Boston, MA, 02114, USA

[5]Weill Cornell Medical College, New York, NY, 10065, USA

Abstract

Purpose—The current study presents [^{18}F]PARPi-FL as a bimodal fluorescent/positron emission tomography (PET) agent for PARP1 imaging.

Procedures—[^{18}F]PARPi-FL was obtained by ^{19}F/^{18}F isotopic exchange and PET experiments, biodistribution studies, surface fluorescence imaging, and autoradiography carried out in a U87 MG glioblastoma mouse model.

Results—[^{18}F]PARPi-FL showed high tumor uptake *in vivo* and *ex vivo* in small xenografts (<2 mm) with both PET and optical imaging technologies. Uptake of [^{18}F]PARPi-FL in blocked U87 MG tumors was reduced by 84 % (0.12±0.02 %injected dose/gram (%ID/g)), showing high specificity of the binding. PET imaging showed accumulation in the tumor (1 h p.i.), which was confirmed by *ex vivo* phosphor autoradiography.

Conclusions—The fluorescent component of [^{18}F]PARPi-FL enables cellular resolution optical imaging, while the radiolabeled component of [^{18}F]PARPi-FL allows whole-body deep-tissue imaging of malignant growth.

Keywords

PARP1; Glioblastoma; PET; Fluorescence; Multimodality; Imaging; U87 MG

Correspondence to: Thomas Reiner; reinert@mskcc.org.
Giuseppe Carlucci and Brandon Carney contributed equally to this work.

Conflict of Interest. The authors report no conflicts of interest.

Authors' Contributions. The manuscript was written through contributions of all authors. All authors have given approval to the final version of the manuscript.

Electronic supplementary material The online version of this article (doi: 10.1007/s11307-015-0858-0) contains supplementary material, which is available to authorized users.

Introduction

Biomedical imaging has revolutionized our understanding of cancer biology, and with it, our ability to examine preclinical models of malignant growth. Intravital fluorescence microscopy can be used to study diverse biological processes at the cellular level [1]. Positron emission tomography (PET) can report on the distribution of cells and drugs on a whole-body level [2]. In the clinic and in medical practice, PET imaging has proven to be an invaluable source of the information necessary for the effective diagnosis and staging of disease [2, 3]. For these reasons, highly specific molecular biomarkers have, along with advancing detection technologies, become increasingly important in the standard of care for cancer treatment [4].

PET in particular has become one of the most prevalent clinical imaging modalities, emerging as one of the key diagnostic tools for whole-body imaging of cancer in the clinic. PET imaging is highly sensitive as well as quantitative and provides a resolution of tumors on a lesion-by-lesion basis. However, the technology does not outperform other imaging technologies in every aspect. PET is expensive, it exposes the patient to ionizing radiation, and it has poor temporal and spatial resolution [5, 6].

Several features of intraoperative fluorescence imaging are orthogonal to PET: the fluorescently emitted light—typically in the visible and near-infrared (NIR) range—is heavily attenuated, which prevents deep-tissue imaging. However, intraoperative fluorescence imaging provides much higher (up to sub-cellular) resolution and has recently been used to add artificial optical contrast during surgical interventions [7, 8]. This technique could become an important tool in the operating room and help to achieve more complete tumor resections, but it still lacks the deep tissue penetration to discover growths buried deep in the patient tissue as PET imaging is able to do.

The creation of targeted bimodal probes, which fuse the benefits of different types of imaging agents, could lead to better and more accurate location of diseased tissue [9, 10]. Target specificity is critical to the efficacy of these probes. Other novel bimodal probes for PET/epifluorescence imaging that target the GLP-1 receptor, a cell surface marker overexpressed in insulinoma, have been described [11]. Other imaging agents make use of the enhanced permeability and retention (EPR) effect [12], which allows an imaging agent to be delivered to lesions via a physiological property rather than the expression of a specific molecular marker [13]. Recently, it was demonstrated that enhanced fluorescent contrast agents facilitate more complete resection of glioblastoma. The use of contrast-enhancing 5-aminolevulinic acid during neurosurgical resections of glioblastoma resulted in a 6-month improved progression-free survival [8].

Artificial bimodal intraoperative and deep tissue contrast could ultimately become particularly important for the surgical resection of glioblastoma, a highly infiltrative disease, where resection often remains incomplete [14–16]. Different reports have shown that the nuclear DNA repair enzyme PARP1 is overexpressed in a variety of diseases and that the expression levels of PARP1 have prognostic value [17–20]. This is evidenced in brain malignancies with elevated rates of PARP1 that contrast significantly with the low PARP1

protein content in healthy brain tissue [21, 22]. Following these findings, we have shown that the elevated PARP1 expression can be exploited to image glioblastoma in mouse models of cancer with PARPi-FL, a fluorescently labeled PARP1-targeted imaging agent [23–25]. Similar to other fluorescent imaging agents, however, the tissue penetration depth of PARPi-FL is limited. Therefore, we hypothesized that a bimodal version of this small molecule would allow the detection of glioblastoma—both non-invasively using PET and at high resolution using fluorescence imaging. The goal of the current study was to use a $^{18}F/^{19}F$ exchange reaction [26–29] to transform the fluorescent PARPi-FL molecule into a structurally identical but PET-active imaging agent, [^{18}F]PARPi-FL [29]. In the current study, we show that the PARPi-FL can be radiolabeled and used to augment the limitations of the "fluorescence only" intraoperative imaging molecule. We predict that a bimodal-targeted PARP1 imaging agent will be beneficial as a standard of care diagnostic agent while also being useful for the identification of surgical tissue margins at high resolution and the deep tissue delineation of malignant growth.

Materials and Methods

A detailed description of synthetic procedures, radiosynthesis, and *in vitro* and *in vivo* experiments can be found in the supplemental data. All animal experiments were done in accordance with protocols approved by the Institutional Animal Care and Use Committee of Memorial Sloan Kettering Cancer Center and followed National Institutes of Health guidelines for animal welfare.

Results

Radiosynthesis of [^{18}F]PARPi-FL1

The molecular structure of PARPi-FL is based on the PARP1 inhibitor Olaparib [25, 30]. Figure 1a (top) shows both the PARP1 targeting 2H-phthalazin-1-one scaffold of the small molecule (blue) as well as its fluorescent BODIPY-FL component (orange). $^{18}F/^{19}F$ trans-fluorination allows one of the BODIPY-FL fluorine atoms to be exchanged with $^{18}F^-$, generating a bimodal, but otherwise structurally identical version of the fluorescent imaging agent (Fig. 1a, bottom). Based on previous reports [26–29], we devised an automated strategy to generate the radiolabeled bimodal [^{18}F]PARPi-FL (Fig. 1b). The $^{18}F/^{19}F$ exchange was facilitated by the Lewis acid $SnCl_4$ (Fig. 2a), yielding the targeted dual-modality imaging agent, as determined by reversed-phase HPLC and confirmed by mass spectrometry (MS) analysis [$C_{34}H_{32}BF_3N_6O_3$: expected ESI-MS=640.2; observed ESI-MS 639.2 ($M\text{-}H^+$); Fig. 2b, Fig. S2]. The manual execution of the $^{19}F/^{18}F$ trans-fluorination yielded specific activities of 2.9±0.7 mCi/μmol, with isolated radiochemical yields of 23 ±8.2 % and radiochemical purities of 85±9.8 %. The manual synthesis required 90 min, including HPLC purification, evaporation of solvents, and formulation of an injectable solution. For the optimization procedure, one condition at a time (time, temperature, concentration of starting material, starting activity, reaction volume, and concentration of $SnCl_4$) was varied in order to find optimal reaction parameters (Fig. 3). Radiochemical yields correlated to the amount of $^{18}F^-$ starting activity (34.8±1.1 % with 45 mCi of $^{18}F^-$). Yields were also seen to increase with decreasing amounts of $SnCl_4$ [40.6±3.3 % with 10 eq.

$SnCl_4$ (μmol)/PARPi-FL (μmol)]. The specific activity was proportional to the activity of added ^{18}F. With increasing temperature and $SnCl_4$, the yields decreased, presumably due to larger fractions of PARPi-FL being subjected to degradation. Longer reaction times did not markedly increase the labeling yield. The automated [^{18}F]PARPi-FL synthesis was beneficial compared to the manual process (Table S1). Based on our screening, we were able to increase the specific activity by 266 % (from 3 to 9 mCi/μmol). The isolated radiochemical yields were increased by 187 % (from 23 to 43 %). Finally, the automated synthetic process was faster, allowing the ^{18}F-PARPi-FL synthesis to be performed in only 70 min (90 min for manual synthesis).

Immunohistochemistry and Autoradiography

Using histological sections of healthy mouse brain and U87 MG glioblastoma xenografts, we showed that the PARP1 expression in the U87 MG tissues is increased by a factor of 11.4 (17.1±1.6 and 1.5±0.9 % PARP1-positive area for U87 MG and healthy mouse brains, respectively, Fig. S4). To probe the selective uptake of [^{18}F]PARPi-FL, we performed autoradiographic staining on resected tissues (U87 MG tumor, brain, muscle) obtained from mice, which were injected with only the [^{18}F]PARPi-FL (non-blocked) or [^{18}F]PARPi-FL 30 min after injection of Olaparib as blocking agent (blocked). Autoradiography showed a homogeneous distribution of radioactivity in the tumors of non-blocked mice (Fig. 4a). The uptake in tumors of blocked mice was markedly lower, with an overall reduction of 80±12 % (Fig. 4b). Hematoxylin and eosin (H&E) staining demonstrated that the retention of radioactive material co-localized with viable tumor tissue. Blocking lowered the [^{18}F]PARPi-FL tumor to muscle ratio by approximately 66 % (7.5±0.9 and 2.6±1.6, $P<0.001$ for non-blocked and blocked mice, respectively). In contrast, the brain to muscle ratio did not undergo statistically significant changes (0.87± 0.48 and 1.02±0.22 for non-blocked and blocked mice, $P= 0.646$, respectively, Fig. 4c).

Surface Fluorescence Imaging

The bimodal imaging capabilities of [^{18}F]PARPi-FL were determined by combined optical/autoradiographic *ex vivo* analysis. The uptake of [^{18}F]PARPi-FL in the tumor was higher than the observed accumulation in brain and muscle in both surface fluorescence imaging (tumor to brain ratio was sevenfold increased) and autoradiography (tumor to brain ratio was ninefold higher) (Fig. 5a–c). The differences in imaging ratios (sevenfold versus ninefold) are likely due to the differences in penetration depths and readout techniques for the two imaging modalities.

Olaparib-blocked organs showed greatly reduced uptake in the tumor (74±12 and 66±9 % reduction for surface fluorescence imaging and autoradiography, respectively). Line profiles of tumors and brains were obtained with both imaging techniques. Autoradiographic staining and epifluorescence imaging provided corresponding organ uptake profiles (Fig. 5d, e). These results indicate that [^{18}F]PARPi-FL should be capable of generating high-contrast bimodal images of tumor tissue and that the tumor to brain ratio is sufficiently high to allow effective imaging of the tracer in the brain during intraoperative imaging procedures.

Small Animal PET Imaging

Small animal PET imaging studies were conducted to investigate [^{18}F]PARPi-FL as a whole-body imaging agent. After administration of 100–200 μl (80–160 mCi/μmol) of the tracer, U87 MG glioblastoma xenografts could be identified in the right shoulder of tumor-bearing mice in both coronal and axial PET/CT reconstructions (Fig. 6a). The uptake of [^{18}F]PARPi-FL in U87 MG tumors was 0.78±0.1, which we were able to reduce to 0.15±0.06 by blocking with an excess of Olaparib (500 mM, 3.7 μmol, in 100 μl 15 % PEG300/85 % 0.9 % saline), similar to what has been done before [24]. The standardized uptake value (SUV) in U87 MG tumors was 1.10±0.53, which also could be reduced to 0.10±0.06 by blocking pre-injection of an excess of Olaparib (50-fold).

PET imaging revealed a high uptake in the liver and in the intestinal tract, which is consistent with hepatobiliary excretion and analogous to what we and others have seen for monomodal radiolabeled PARP1 imaging agents [31, 32] (Fig. 6a, b). Activity was also observed in the bone and junctures, typically a result of defluorination of radiolabeled imaging agents during metabolic degradation.

Blood Half-Life and Biodistribution

In order to explore the potential *in vivo* applications of [^{18}F]PARPi-FL as a multimodality imaging probe, we evaluated its blood half-life (Fig. 6c). After tail vein injection of [^{18}F]PARPi-FL (27 μCi, 100 μl), the observed weighted $t_{1/2}$ was 15.6 min. The calculated tumor uptake in the positive control group, at 90 min p.i., was 0.78±0.1 %injected dose/gram (%ID/g). Tumor uptake dropped to 0.1±0.02 %ID/g at 90 min p.i. for mice that received a pre-injection of Olaparib. For each group, liver and kidney uptake of the radiotracer was lower in mice receiving a pre-injection of Olaparib, indicating specific binding of the tracer to a certain extent additionally to the uptake due to excretion. (Liver 3.8±0.4 and 2.02± 0.2 %ID/g, $P<0.001$ and kidneys 0.7±0.1 and 0.4±0.1 %ID/g, $P<0.05$, for non-blocked and blocked, respectively) (Fig. 6d). The tumor to muscle ratio of [^{18}F]PARPi-FL was 4±0.6 at 90 min post injection. The tumor to brain tissue ratio of 12±2.1 (Fig. 6e) indicates a significant potential clinical value for the probe.

Discussion

The primary objective of this study was to explore the synthesis and *in vivo* pharmacokinetics of [^{18}F]PARPi-FL as a potential bimodal PET/optical imaging agent for PARP1-targeted imaging of glioblastoma. In recent years, PARP1 therapeutics have been a major focus in biomedical and pharmaceutical research [33, 34]. This focus is reflected in the number of PARP1 therapeutics which are currently being evaluated in clinical trials (e.g., the three PARP1 therapeutics Olaparib [35], Niraparib [36], and BMN673 [37] have entered phase III trials). Moreover, Olaparib (Lynparza™) was recently approved as a monotherapy for patients with advanced ovarian cancer by the FDA. In addition to the therapeutic value of PARP1 inhibition, the enzyme may also prove to be a valuable target for diagnostic and prognostic tools. It has already been shown to be a powerful diagnostic target for the delineation of glioblastoma [21, 22], [24]. Our central hypothesis is that an ^{18}F-labeled PARPi-FL might enable imaging of brain tumors with high contrast values,

even if their growth in the clinic is highly diffuse and poorly differentiated [38, 39]. $SnCl_4$ was used to facilitate the $^{19}F/^{18}F$ trans-fluorination of the BODIPY-FL group on the PARP1 tracer. The Lewis acid, together with the starting activity of $^{18}F^-$, has been confirmed to be one of the critical parameters in the tracer synthesis. Increasing amounts of $SnCl_4$ cause an increase in specific activity (5.02±0.56 for 50 eq. $SnCl_4$ versus 8.55±0.35 for 150 eq. $SnCl_4$), which might be due to increased degradation of the starting material before ^{18}F is added to the mixture. This is also confirmed by decreasing radiochemical yields (Fig. 3). Similar effects were described and observed by Conti and colleagues [26], and we observed high amounts of radiolabeled, as well as cold by-product formation, with increasing amounts of added $SnCl_4$. Similarly, the amount of [^{18}F]fluoride (n.c.a.) effects both radiochemical yield and specific activity because increasing ratios of $^{18}F/^{19}F$ will also increase the probability of successful incorporation of the isotope. In agreement with expectation, the radiochemical yield and specific activity were both highly dependent on reaction volume (and therefore reactant concentration). For both reaction time and temperature, there are optimal values in which there is enough time and energy for the reaction to proceed without side-product formation to become a dominant reaction pathway.

It was our aim to develop an automated “one-pot” procedure for the synthesis of ^{18}F-PARPi-FL. A one-pot strategy is desired for radiochemical synthesis with short-lived isotopes, which typically reduces the overall synthesis time and results in higher isolated radiochemical yields. Using the values obtained in the optimization procedure, the tracer was synthesized, purified, and formulated within 70 min, using an automated reaction protocol, allowing for clinical translation. The replacement of a ^{19}F with an ^{18}F isotope quickly yielded the final product with a good radiochemical yield (around 30.3±7.3 % dcRCY) and high radiochemical purity (≥98 %). The specific activity was below 200 mCi/μmol, similar to other previously observed $^{18}F/^{19}F$ trans-fluorinations [26]. The lower specific activity of [^{18}F]^{18}F-PARPi-FL relative to other clinical ^{18}F-labeled PET imaging agents is due to structural equivalence of the precursor PARPi-FL and the radiolabeled product, which makes separation not possible. Its specific activity, however, does not reduce the value of this tracer since a bimodal optical/PET imaging agent requires higher concentrations than a monomodal PET agent to obtain sufficient signal/noise ratios in the optical imaging modality. Other studies have used bimodal ^{18}F-labeled and fluorescent PET tracers with specific activities >3 Ci/μmol [40]. Here, the uptake of radiotracer could not be correlated to the optical imaging agent unless cold fluorescent tracer was co-injected [40]. This illustrates that for bimodal parallel imaging of optical and radiolabeled probes, the specific activities might have to be adjusted to the less sensitive imaging modality.

In U87 MG glioblastoma xenograft-bearing mice, ^{18}F-PARPi-FL was rapidly cleared from all organs via the liver, suggesting that the major excretion pathway occurs via hepatobiliary clearance, similar to what is observed for the parent molecule Olaparib [41, 42] and other [^{18}F]BODIPY tracers [43]. One drawback of [^{18}F]PARPi-FL was in the quick metabolic defluorination of the tracer, which results in increased bone uptake (Fig. 5d, e, Table S2). This is in agreement with the known chemistry of BODIPY dyes [44, 45]. Defluorination might limit the broad applicability of the imaging agent. However, the rate of defluorination and the resulting bone uptake might be reduced *in vivo* by addition of cytochrome P450

isozyme 2E1 (CYP2E1) inhibitors, similar to what has been shown before [46–48]. Nevertheless, we were able to show that [^{18}F]PARPi-FL is a potentially valuable, clinically relevant bimodal contrast agent that fuses optical and PET imaging, combining the advantages of whole-body and high-resolution imaging.

Conclusion

This study presents the automated synthesis of a fluorescent/radiolabeled small molecule for imaging of PARP1 *in vivo*—using both epifluorescence and whole-body imaging techniques. We present here an optimized and automated synthesis of this bimodal tracer as well as its *in vivo* properties. The fluorescent sister imaging agent PARPi-FL has been previously demonstrated to be a valuable and selective probe [23–25]. Our radiolabeled, but otherwise structurally identical bimodal version of PARPi-FL, [^{18}F]PARPi-FL, has proven to maintain similar specific binding properties to PARP1 *in vivo* with a comparable uptake and retention behavior to the non-radiolabeled version of the probe.

Radiolabeled fluorescent [^{18}F]PARPi-FL possesses ideal pharmacokinetic properties to detect and interrogate tumor growth and treatment success. It represents a fusion of two widely used imaging technologies in laboratory and diagnostic medicine—PET and fluorescence imaging. The use of a PARP1 imaging agent is particularly valuable for investigating malignant growth in the brain because of the low PARP1 expression in healthy brain tissue that facilitates particularly high signal/noise ratios [17, 21, 22, 46, 47].

In conclusion, we have successfully automated and tested the first PARP1-targeted bimodal imaging agent. We believe that this imaging agent could become useful as an intraoperative fluorescent tool for glioblastoma, where the fluorescent component of [^{18}F]PARPi-FL will allow cellular resolution point-of-care imaging to accurately and non-invasively interrogate surgical margins. At the same time, the radiolabeled component of [^{18}F]PARPi-FL allows for detection of deep-seated lesions below the tissue surface and might be useful in planning radiation treatment. Ultimately, this agent may fulfill unmet clinical needs and assist in the clinical decision-making process.

Supplementary Material

Refer to Web version on PubMed Central for supplementary material.

Acknowledgments

The authors thank Drs. Ralph Weissleder (Harvard Medical School), NagaVaraKishore Pillarsetty (MSKCC), and Jason S. Lewis (MSKCC) for helpful discussions. They also thank Beatriz Salinas-Rodriguez for technical assistance, Valerie Longo for assisting with animal experiments, and David Gregory for critical reading of the manuscript. Support was provided by the Animal Imaging Core Facility, the Radiochemistry and Molecular Imaging Probe Core, as well as the Molecular Cytology Core at Memorial Sloan Kettering Cancer Center (P30 CA008748). This work was made possible by a financial contribution from American Italian Cancer Foundation (AICF) and the Clinical and Translational Science Center (CTSC) at Weill Cornell Medical College (NIH/NCATS Grant TL1TR000459). Finally, the authors thank the National Science Foundation Integrative Graduate Education and Research Trainee-ship (IGERT 0965983 at Hunter College), the NIH (K25EB016673 for T.R.), the Brain Tumor Center of Memorial Sloan Kettering Cancer Center (for T.R.), and the Radiology Development Fund (for T.R.) for their generous funding.

References

1. Pittet Mikael J, Weissleder R. Intravital imaging. Cell. 2011; 147:983–991. [PubMed: 22118457]
2. Neves AA, Brindle KM. Assessing responses to cancer therapy using molecular imaging. Biochim Biophys Acta. 2006; 1766:242–261. [PubMed: 17140737]
3. Torigian DA, Huang SS, Houseni M, Alavi A. Functional imaging of cancer with emphasis on molecular techniques. CA Cancer J Clin. 2007; 57:206–224. [PubMed: 17626118]
4. Weissleder R, Pittet MJ. Imaging in the era of molecular oncology. Nature. 2008; 452:580–589. [PubMed: 18385732]
5. Condeelis J, Weissleder R. In vivo imaging in cancer. Cold Spring Harb Perspect Biol. 2010; 2:a003848–a003848. [PubMed: 20861158]
6. Alford R, Ogawa M, Choyke PL, Kobayashi H. Molecular probes for the in vivo imaging of cancer. Mol Biosyst. 2009; 5:1279–1291. [PubMed: 19823742]
7. van Dam GM, Themelis G, Crane LMA, et al. Intraoperative tumor-specific fluorescence imaging in ovarian cancer by folate receptor-α targeting: first in-human results. Nat Med. 2011; 17:1315–1319. [PubMed: 21926976]
8. Stummer W, Pichlmeier U, Meinel T, et al. Fluorescence-guided surgery with 5-aminolevulinic acid for resection of malignant glioma: a randomised controlled multicentre phase III trial. Lancet Oncol. 2006; 7:392–401. [PubMed: 16648043]
9. Jennings LE, Long NJ. 'Two is better than one'—probes for dual-modality molecular imaging. Chem Commun. 2009; 24:3511–3524.
10. Louie A. Multimodality imaging probes: design and challenges. Chem Rev. 2010; 110:3146–3195. [PubMed: 20225900]
11. Brand C, Abdel-Atti D, Zhang Y, et al. In vivo imaging of GLP-1R with a targeted bimodal PET/Fluorescence imaging agent. Bioconjug Chem. 2014; 25:1323–1330. [PubMed: 24856928]
12. Maeda H, Nakamura H, Fang J. The EPR effect for macromolecular drug delivery to solid tumors: improvement of tumor uptake, lowering of systemic toxicity, and distinct tumor imaging in vivo. Adv Drug Deliv Rev. 2013; 65:71–79. [PubMed: 23088862]
13. Pérez-Medina C, Abdel-Atti D, Zhang Y, et al. A modular labeling strategy for in vivo PET and near-infrared fluorescence imaging of nanoparticle tumor targeting. J Nucl Med. 2014; 55:1706–1711. [PubMed: 25060196]
14. Sanai N, Berger MS. Glioma extent of resection and its impact on patient outcome. Neurosurgery. 2008; 62:753–764. [PubMed: 18496181]
15. Pouratian N, Asthagiri A, Jagannathan J, et al. Surgery insight: the role of surgery in the management of low-grade gliomas. Nat Clin Pract Neurol. 2007; 3:628–639. [PubMed: 17982433]
16. Roberts DW, Valdés PA, Harris BT, et al. Glioblastoma multiforme treatment with clinical trials for surgical resection (aminolevulinic acid). Neurosurg Clin N Am. 2012; 23:371–377. [PubMed: 22748650]
17. Ossovskaya V, Koo IC, Kaldjian EP, et al. Upregulation of poly (ADP-ribose) polymerase-1 (PARP1) in triple-negative breast cancer and other primary human tumor types. Genes Cancer. 2010; 1:812–821. [PubMed: 21779467]
18. Bièche I, de Murcia G, Lidereau R. Poly(ADP-ribose) polymerase gene expression status and genomic instability in human breast cancer. Clin Cancer Res. 1996; 2:1163–1167. [PubMed: 9816283]
19. Rojo F, García-Parra J, Zazo S, et al. Nuclear PARP-1 protein overexpression is associated with poor overall survival in early breast cancer. Ann Oncol. 2012; 23:1156–1164. [PubMed: 21908496]
20. Alanazi M, Pathan AAK, Abduljaleel Z, et al. Association between PARP-1 V762A polymorphism and breast cancer susceptibility in Saudi population. PLoS One. 2013; 3:e92360.
21. Galia A, Calogero AE, Condorelli R, et al. PARP-1 protein expression in glioblastoma multiforme. Eur J Histochem: EJH. 2012; 56:e9. [PubMed: 22472897]
22. Barton VN, Donson AM, Kleinschmidt-DeMasters BK, et al. PARP1 expression in pediatric central nervous system tumors. Pediatr Blood Cancer. 2009; 53:1227–1230. [PubMed: 19533660]

23. Thurber GM, Yang KS, Reiner T, et al. Single-cell and subcellular pharmacokinetic imaging allows insight into drug action in vivo. Nat Commun. 2013; 4:1504. [PubMed: 23422672]
24. Irwin CP, Portorreal Y, Brand C, et al. PARPi-FL—a fluorescent PARP1 inhibitor for glioblastoma imaging. Neoplasia. 2014; 16:432–440. [PubMed: 24970386]
25. Reiner T, Lacy J, Keliher EJ, et al. Imaging therapeutic PARP inhibition in vivo through bioorthogonally developed companion imaging agents. Neoplasia. 2012; 14:169–177. [PubMed: 22496617]
26. Liu S, Lin T-P, Li D, et al. Lewis acid-assisted isotopic ^{18}F-^{19}F exchange in BODIPY dyes: facile generation of positron emission tomography/fluorescence dual modality agents for tumor imaging. Theranostics. 2013; 3:181–189. [PubMed: 23471211]
27. Li Z, Lin T-P, Liu S, et al. Rapid aqueous [^{18}F]-labeling of a BODIPY dye for positron emission tomography/fluorescence dual modality imaging. Chem Commun. 2011; 47:9324–9326.
28. Hendricks JA, Keliher EJ, Wan D, et al. Synthesis of [^{18}F]BODIPY: bifunctional reporter for hybrid optical/positron emission tomography imaging. Angew Chem. 2012; 51:4603–4606. [PubMed: 22473535]
29. Keliher EJ, Klubnick JA, Reiner T, et al. Efficient acid-catalyzed ^{18}F/^{19}F fluoride exchange of BODIPY dyes. ChemMedChem. 2014; 9:1368–1373. [PubMed: 24596307]
30. Menear KA, Adcock C, Boulter R, et al. 4-[3-(4-Cyclopropanecarbonylpiperazine-1-carbonyl)-4-fluorobenzyl]-2H-phthalazin-1-one: a novel bioavailable inhibitor of poly(ADP-ribose) polymerase-1. J Med Chem. 2008; 51:6581–6591. [PubMed: 18800822]
31. Zhou D, Chu W, Xu J, et al. Synthesis, [^{18}F] radiolabeling, and evaluation of poly (ADP-ribose) polymerase-1 (PARP-1) inhibitors for in vivo imaging of PARP-1 using positron emission tomography. Bioorg Med Chem. 2014; 22:1700–1707. [PubMed: 24503274]
32. Keliher EJ, Reiner T, Turetsky A, et al. High-yielding, two-step ^{18}F labeling strategy for ^{18}F-PARP1 inhibitors. ChemMedChem. 2011; 6:424–427. [PubMed: 21360818]
33. Sonnenblick A, de Azambuja E, Azim HA, Piccart M. An update on PARP inhibitors-moving to the adjuvant setting. Nat Rev Clin Oncol. 2014; 12:27–41. [PubMed: 25286972]
34. Li M, Yu X. The role of poly(ADP-ribosyl)ation in DNA damage response and cancer chemotherapy. Oncogene. 2014; 1:8.
35. Ledermann J, Harter P, Gourley C, et al. Olaparib maintenance therapy in patients with platinum-sensitive relapsed serous ovarian cancer: a preplanned retrospective analysis of outcomes by BRCA status in a randomised phase 2 trial. Lancet Oncol. 2014; 15:852–861. [PubMed: 24882434]
36. Sandhu SK, Schelman WR, Wilding G, et al. The poly(ADP-ribose) polymerase inhibitor niraparib (MK4827) in BRCA mutation carriers and patients with sporadic cancer: a phase 1 dose-escalation trial. Lancet Oncol. 14:882–892. [PubMed: 23810788]
37. Murai J, Huang S-YN, Renaud A, et al. Stereospecific PARP trapping by BMN 673 and comparison with Olaparib and Rucaparib. Mol Cancer Ther. 2014; 13:433–443. [PubMed: 24356813]
38. Miller CR, Perry A. Glioblastoma. Arch Pathol Lab Med. 2007; 131:397–406. [PubMed: 17516742]
39. Louis DN, Ohgaki H, Wiestler OD, et al. The 2007 WHO classification of tumours of the central nervous system. Acta Neuropathol. 2007; 114:97–109. [PubMed: 17618441]
40. Liu Z, Radtke MA, Wong MQ, et al. Dual mode fluorescent ^{18}F-PET tracers: efficient modular synthesis of rhodamine-[cRGD]2-[^{18}F]-organotrifluoroborate, rapid, and high yielding one-step ^{18}F-labeling at high specific activity, and correlated in vivoPET imaging and *ex vivo* fluorescence. Bioconjug Chem. 2014; 25:1951–1962. [PubMed: 25265337]
41. Murai J, Huang SN, Das BB, et al. Trapping of PARP1 and PARP2 by clinical PARP inhibitors. Cancer Res. 2012; 72:5588–5599. [PubMed: 23118055]
42. Chen Y, Zhang L, Hao Q. Olaparib: a promising PARP inhibitor in ovarian cancer therapy. Arch Gynecol Obstet. 2013; 288:367–374. [PubMed: 23619942]
43. Liu S, Li D, Zhang Z, et al. Efficient synthesis of fluorescent-PET probes based on [^{18}F]BODIPY dye. Chem Commun. 2014; 50:7371–7373.

44. Hecht M, Fischer T, Dietrich P, et al. Fluorinated boron-dipyrromethene (BODIPY) dyes: bright and versatile probes for surface analysis. Chem Open. 2013; 2:25–38.

45. Lakshmi V, Chatterjee T, Ravikanth M. Lewis acid assisted decomplexation of F-BODIPYs to dipyrrins. Eur J Org Chem. 2014; 2014:2105–2110.

46. Thurber GM, Reiner T, Yang KS, et al. Effect of small-molecule modification on single-cell pharmacokinetics of PARP inhibitors. Mol Cancer Ther. 2014; 13:986–995. [PubMed: 24552776]

47. Kharasch ED, Thummel KE. Identification of cytochrome P450 2E1 as the predominant enzyme catalyzing human liver microsomal defluorination of sevoflurane, isoflurane and methroxyflurane. Anesthesiology. 1993; 79:795. [PubMed: 8214760]

48. Ryu YH, Liow JS, Zoghbi S, et al. Disulfiram inhibits defluorination of (18)F-FCWAY, reduces bone radioactivity, and enhances visualization of radioligand binding to serotonin 5-HT1A receptors in human brain. J Nucl Med. 2007; 48:1154. [PubMed: 17574977]

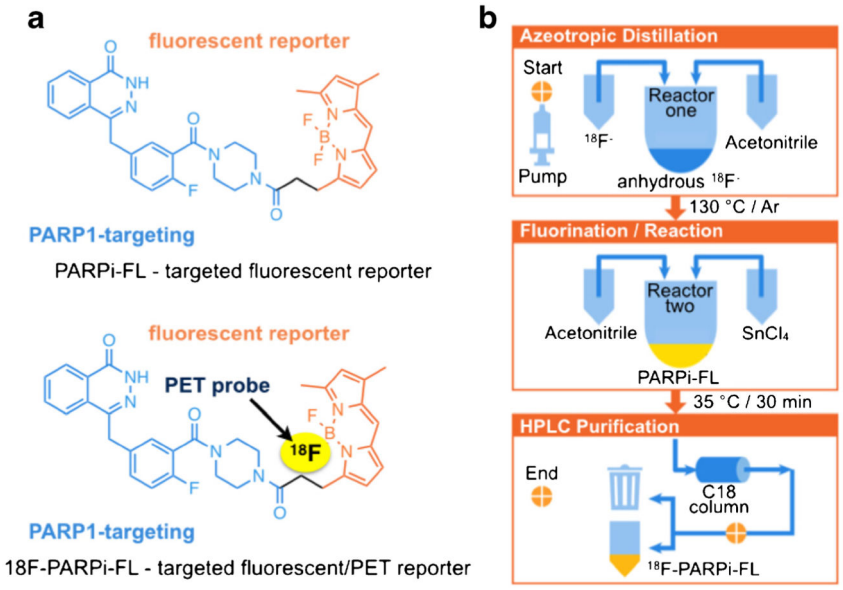

Fig. 1.

Structure of [^{18}F]PARPi-FL and schematic for the automated synthesis: **a** structures of the fluorescent monomodal and ^{18}F-labeled bimodal PARP1 targeted probes and **b** the synthesis of [^{18}F]PARPi-FL is automated and performed in an ^{18}F synthesis module. The *upper panel* shows the azeotropic distillation. The *middle panel* illustrates the fluorination/reaction step, followed by HPLC purification (*lower panel*).

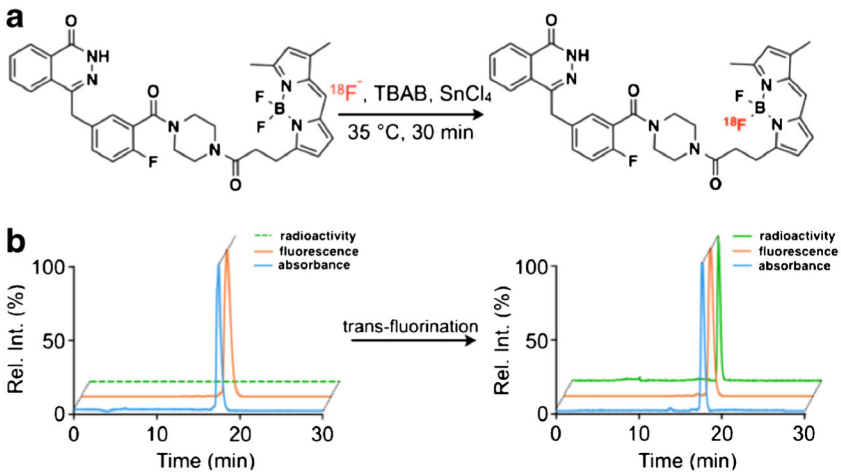

Fig. 2.

a Radiochemical synthesis diagram for [^{18}F]PARPi-FL. The ^{18}F/^{19}F exchange was realized in the presence of $SnCl_4$ at 35 °C for 30 min. [^{18}F]PARPi-FL was purified by reversed-phase high-performance liquid chromatography (RP-HPLC); **b** representative HPLC chromatograms traces (radioactivity, fluorescence, and absorbance) show the trans-fluorination of [^{19}F]PARPi-FL to [^{18}F]PARPi-FL.

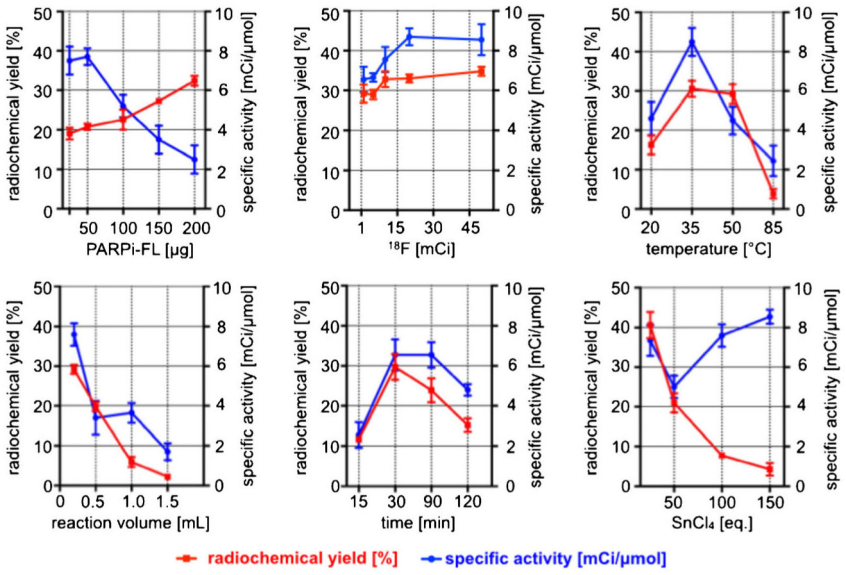

Fig. 3.

Optimization of [^{18}F]PARPi-FL synthesis. Several conditions were tested and the radiochemical yields and specific activity determined for each condition (each data point represents the average of three individual runs). Standard conditions: 50 µg PARPi-FL, 10 mCi of ^{18}F, 35 °C, 0.2 ml, 30 min, 10 eq. $SnCl_4$. Radiochemical yields are decay corrected.

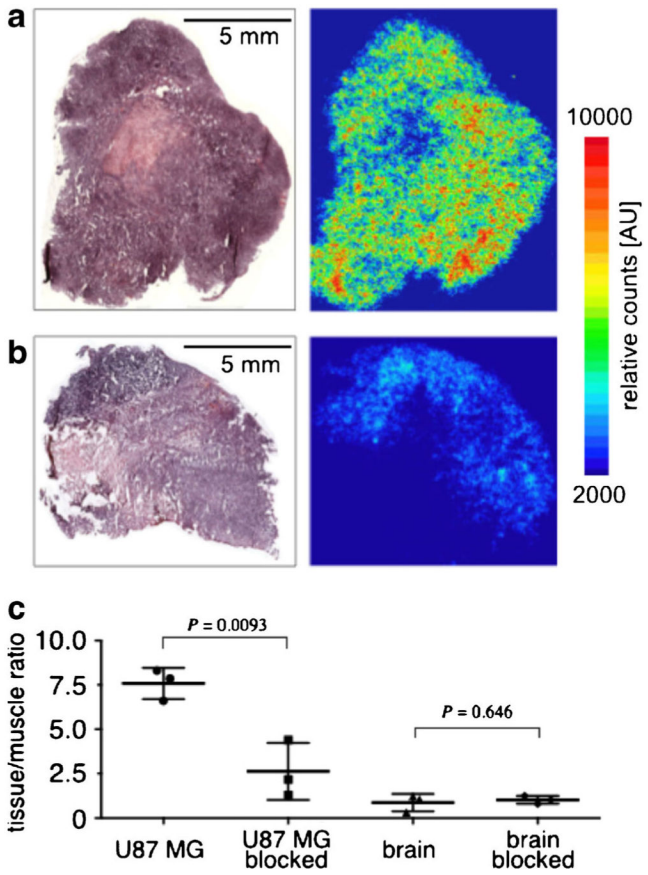

Fig. 4.

H&E staining (*left panels*) and autoradiography (*right panels*) of **a** positive and **b** blocked U87 MG tumor slices; **c** tissue/muscle ratio calculated for tumors (positive and blocked) and brains (positive and blocked).

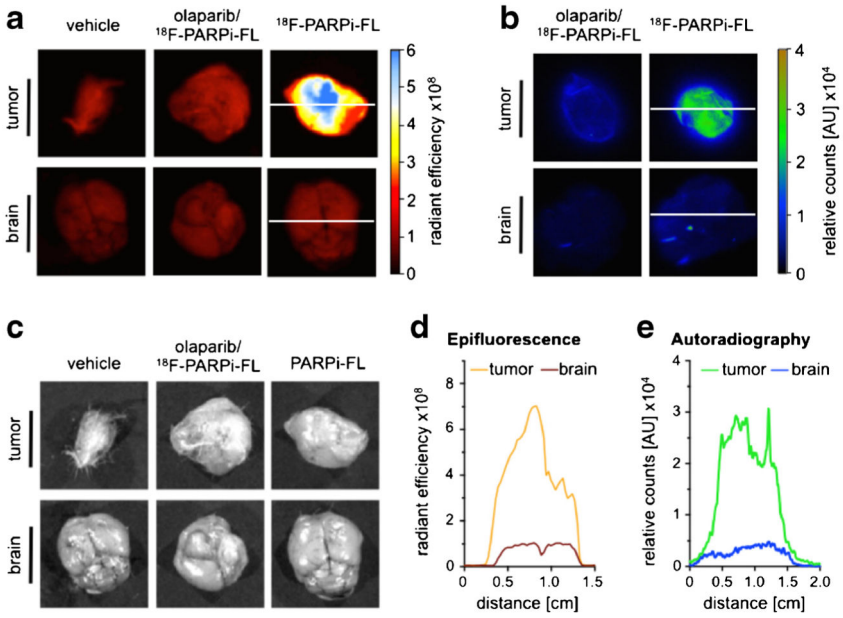

Fig. 5.

$^{18}[^{18}F]$PARPi-FL tumor accumulation and PARP1 expression; **a** representative images of tumor and brain tissue obtained by IVIS optical imaging, including the corresponding **b** autoradiography and **c** white light images; **d** fluorescence intensity profiles across tumor and brain and **e** autoradiographic profile plot of the same organs. Radiant efficiency=emission light (photons/s/cm^2/str)/excitation light (mW/cm^2). *White lines* in panels (**a**) and (**b**) indicate the data used for the profiles in panel (**d**).

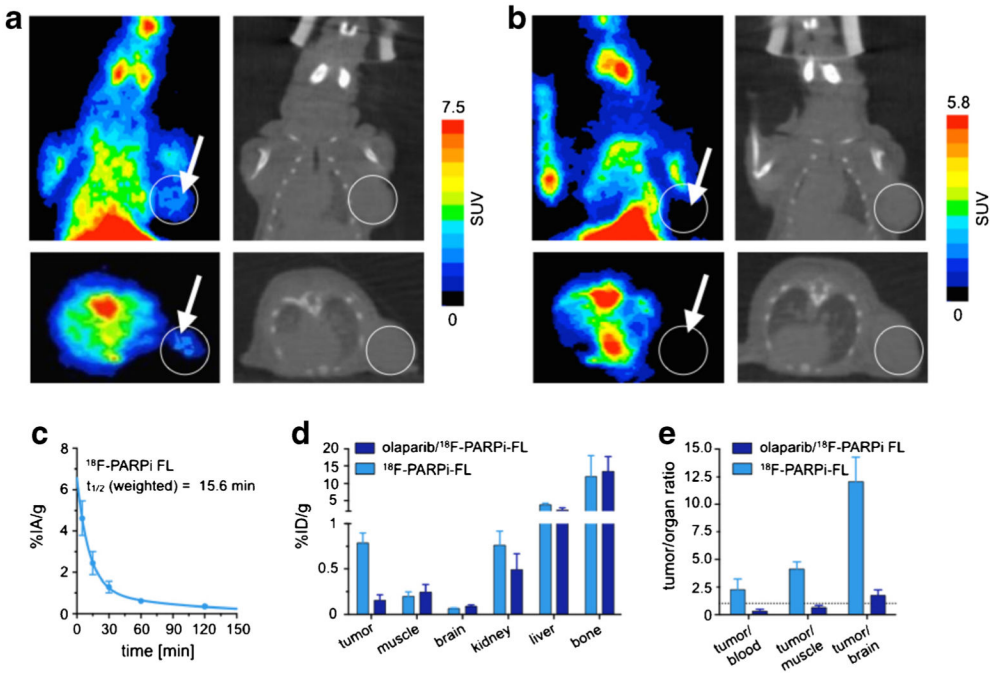

Fig. 6.

a PET coronal and axial images (left) and corresponding CT images (*right*) of a mouse injected with [^{18}F]PARPi-FL (200 μCi in 100 μl 15 % PEG300/85 % 0.9 % saline); **b** PET coronal and axial images (*left*) and corresponding CT images (*right*) after pre-injection of blocking agent; **c** *ex vivo* blood half-life of [^{18}F]PARPi-FL (*n* =4). Blood was collected at different time points (5, 15, 30, 60, and 120 min), weighed, and γ-counted. Results expressed as percent injected activity/gram (%IA/g); **d** biodistribution study in selected tissues. After injection of [^{18}F]PARPi-FL into tumor xenograft mice, mice were euthanized and the radioactivity in the organs was counted (*n* =4); **e** selected tumor to non-target tissues ratio of [^{18}F]PARPi-FL. Radioactivity in tissues is expressed as percent injected dose/gram. *Error bars* indicate standard deviation (*n* =4).